Electron-Beam-Driven Devices With Synchronous Multiple Degenerate Eigenmodes

Ahmed F. Abdelshafy, Mohamed A. K. Othman, *Member, IEEE*, Farshad Yazdi, Mehdi Veysi, Alexander Figotin, and Filippo Capolino, *Senior Member, IEEE*

***Abstract*— We provide here a comprehensive exposition of a novel dispersion engineering framework for high-power electron-beam-driven devices based on multiple degenerate eigenwave synchronization in slow-wave structures (SWSs). These degenerate eigenwaves, related to an exceptional point of degeneracy (EPD) in the parameter space of the SWSs, lead to an enhanced interaction with the electron beam associated with a vanishing group velocity, which depends on the EPD order. Therefore, a "supersynchronous" mechanism based on multiple degenerate eigenwaves, associated with any order of EPD, provides advantages in terms of power generation efficiency at microwave frequencies, millimeter-wave frequencies, and terahertz frequencies. We present a physical description of EPDs in SWSs using a generalized Pierce theory developed for multimodal interaction. We show unique characteristics related to EPDs in "hot" (coupled with the electron beam) SWSs with third- and fourth-order EPDs for the sake of demonstration, but this can be extended to any order of degeneracy. We demonstrate advantages of the proposed regimes compared to conventional single-mode high-power devices such as backward-wave oscillators and traveling-wave tube amplifiers. In addition to that we show a possibility of high-power oscillators at millimeter-wave and terahertz frequencies based on a fourth-order EPD. In particular, we demonstrate a degenerate band-edge oscillator at 638 GHz based on particle-in-cell simulations. Apart from the examples provided herein, the concept of EPD can be used to design a wide variety of devices including gyrotrons, free electron lasers, and high-power isolators.**

***Index Terms*— Backward-wave oscillators (BWO), dispersion engineering, high-power microwave, slow-wave structure (SWS).**

I. Introduction

GENERATION of high-power microwaves has received increasing interest due to the increasing demand of compact powerful sources for various applications. Electron-beam-driven devices such as traveling-wave tubes (TWTs), magnetron, and backward-wave oscillators (BWOs) are the most utilized, commercially available high-power sources due to their simple design, suitable levels of power, and well-established technology [1]. TWTs and BWO are based on the coherent interaction of electromagnetic (EM) waves in a slow-wave structure (SWS) with a synchronous electron beam (see [2, Ch. 8]). The performance of the state-of-the-art high TWTs and BWO is fundamentally limited by the interaction efficiency between the beam and the EM wave, thus mandates the power generation efficiency, bandwidth, and size. Dispersion engineering of eigenmodes in SWSs is a procedure, whereby the dispersion diagram, field properties, and interaction impedance are leveraged, proving the favorable conditions for an enhanced interaction with the electron beam. Several concepts and designs of SWSs for an effective interaction with the electron beam and consequent performance enhancement have been recently investigated [3]–[9]. High-power generation at millimeter-wave and terahertz frequencies poses significant challenges related to power handling and mode control. Moreover, due to device dimensions and limitations of current fabrication technologies [10], [11], generating of high power at millimeter-wave and terahertz frequencies is very challenging. The novel characteristics in SWSs with unprecedented dispersion properties can be harvested to achieve the anticipated mode control and coherent radiation.

In this paper, we provide a comprehensive overview of a new operational principle in high-power amplifiers and oscillators where multiple degenerate EM eigenwaves interact synchronously with an electron beam. The special condition of having multiple degenerate modes in an SWS is related to the concept of the exceptional point of degeneracy (EPD). The EPD is a point in the parameter space of an SWS associated with the coalescence of Floquet–Bloch eigenmodes (or eigenwaves) into a single one. Note that this is a strong degeneracy condition; it is a stronger condition than having eigenmodes in an SWS with the same wavenumber. At the EPD, multiple modes of the periodic structure become indistinguishable. EPDs could be found or engineered in various waveguiding structures and could possess different orders, namely, a different number of coalescing eigenmodes. In a cold and lossless SWS, a fourth-order EPD condition, for instance, is often referred to as the degenerate band edge (DBE), whereas a third-order EPD is referred to a stationary inflection points (SIP). Ideal EPD conditions are realizable in periodic structures without losses and gain. At both the DBE and

Manuscript received January 30, 2018; revised May 24, 2018; accepted June 28, 2018. Date of publication July 6, 2018; date of current version August 9, 2018. This work was supported by the Air Force Office of Scientific Research under the Multidisciplinary University Research Initiative award number FA9550-12-1-0489 administered through the University of New Mexico and under award number FA9550-15-1-0280. The review of this paper was arranged by Senior Editor S. J. Gitomer. *(Corresponding author: Filippo Capolino.)*

A. F. Abdelshafy, M. A. K. Othman, F. Yazdi, M. Veysi, and F. Capolino are with the Department of Electrical Engineering and Computer Science, University of California, Irvine, CA 92697 USA (e-mail: abdelsha@uci.edu; mothman@uci.edu; f.capolino@uci.edu).

A. Figotin is with the Department of Mathematics, University of California, Irvine, CA 92697 USA (e-mail: afigotin@uci.edu).

Color versions of one or more of the figures in this paper are available online at http://ieeexplore.ieee.org.

Digital Object Identifier 10.1109/TPS.2018.2852733

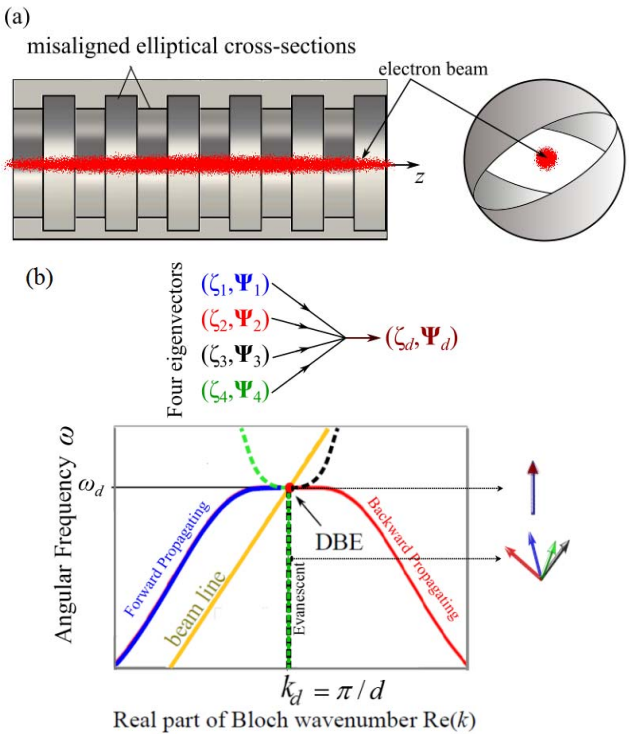

Fig. 1. (a) Example of SWS with EPD where multiple Floquet–Bloch eigenwaves coalesce into a single degenerate one. (b) Typical dispersion diagram near the DBE of the Floquet–Bloch eigenwaves in an SWS as in (a). Four Floquet–Bloch eigenmodes represented by their eigenvectors $\mathbf{\Psi}_n$ and eigenvalues ζ_n with $n = \{1, 2, 3, 4\}$ are graphically represented as vectors: two eigenvectors represent propagating eigenwaves and the other two represent evanescent eigenwaves below the DBE angular frequency ω_d. The four eigenvectors coalesce at the DBE in both eigenvectors, namely, $\mathbf{\Psi}_d$ and eigenvalues ζ_d. Supersynchronization occurs when the phase velocity of the multiple degenerate eigenwaves in the SWS matches the velocity u_0 of the electron-beam charge wave. This is shown graphically in this figure by the intersection of the beamline with the cold structure dispersion at the DBE frequency satisfying the four-mode synchronization condition $\omega_d \approx k_d u_0$.

the SIP, the group velocity vanishes and unique slow-wave resonance features occur [12]–[18]. The DBE that is realized in periodic waveguide structures supports two polarization states with the capability of mixing them periodically along the z-direction [12], [13], [19], [20]. The DBE is observed in the waveguide example in Fig. 1(a) comprised corrugations with misaligned elliptic cross section. Such slow-wave properties have elicited growing interest for applications such antenna and delay lines [21]–[24]. Othman *et al.* [17], [18], [25] have proposed a supersynchronous regime in SWSs when multiple, degenerate eigenwaves interact with a synchronous electron beam that lead to a giant gain enhancement and low-starting current in oscillators.

Here, we present a general framework describing the properties and functionality of EPDs in high-power electron-beam-driven structures. EPDs like the DBE and the SIP where initially discovered in lossless photonic crystals [12], [14], [26]. However, EPDs are also attainable in structures with gain and loss or with parity-time symmetry [27]–[32], and may be utilized also in the high-power generation contest. The advanced operational principle based on EPD conditions may lead to phenomenological advantages in mode control and oscillating mode selection, leading to power efficiency in high-power amplifiers and oscillators. In Section II, we summarize the eigenwave formulation in "cold" SWSs (i.e., without the electron beam) that support multiple Bloch–Floquet eigenwaves, as shown in Fig. 2. In Section III, we show the some realistic examples of waveguides with EPD, and we also show the experimental results to verify such concepts. In Section IV, we provide a comprehensive framework for the generalized Pierce theory for SWSs with EPDs interacting with an electron beam and study: 1) low-starting oscillation current in DBE oscillators (DBEOs) and 2) efficient and wideband amplification in TWTs with SIP. In Section V, we investigate other regimes of operation for high-power generation using EPDs at millimeter-wave and terahertz frequencies, we show the existence of the DBE in two structures, and we demonstrate our first result based on full-wave simulations of a DBEO at terahertz frequency.

II. Exceptional Points of Degeneracy and Dispersion Engineering

An EPD occurs when EM eigenmodes in an SWS coalesce into a single eigenmode when varying frequency or other structural parameters of the waveguide (see [33, Ch. 2]) [34], [35]. EPDs are different from simple degenerate modes in waveguides. The latter so-called "degeneracy" means that two eigenmodes have the same eigenvalue (wavenumber) but different field distributions (e.g., two TE11 or two TM11 modes in a rectangular waveguide with orthogonal transverse field polarizations) (see [36, Ch. 3]). On the contrary, an EPD is a degeneracy condition that includes also the degeneracy of polarization states of the system (i.e., the eigenvectors) in addition to coincident eigenvalues. EPDs occur in lossless periodic structures at a frequency that separates the EM bandgap from the passband in the spectrum of eigenwaves, which would not be attainable in uniform waveguides. The DBE is a fourth-order EPD that occurs when all four independent Floquet–Bloch eigenvectors in lossless periodically coupled waveguides coalesce and form one single eigenvector [12], [26], [37] at the band edge. In the following, we provide a concise description of the EPD occurring in SWS modeled by coupled-transmission lines (CTLs).

A. Coupled-Transmission Line Formulation

Without the loss of generality of the subsequent analysis, we refer to a periodic SWS with multiple Floquet–Bloch eigenwaves as shown in Fig. 1(a). What is discussed in this paper can be applied to several other examples of SWS. Field propagation in the example of "cold" SWS shown in Fig. 2(a) can be equivalently described using the CTL model in Fig. 2(b) and (c). It is composed of cascaded sections of misaligned elliptical waveguides. Each waveguide section has an elliptic cross section, and wave propagation in each section is the same except for an angular rotation in the xy plane. The following description also applies to other geometries with EPDs [19], [38].

In general, guided waves in closed waveguides are represented via transverse electric and magnetic fields, and voltages

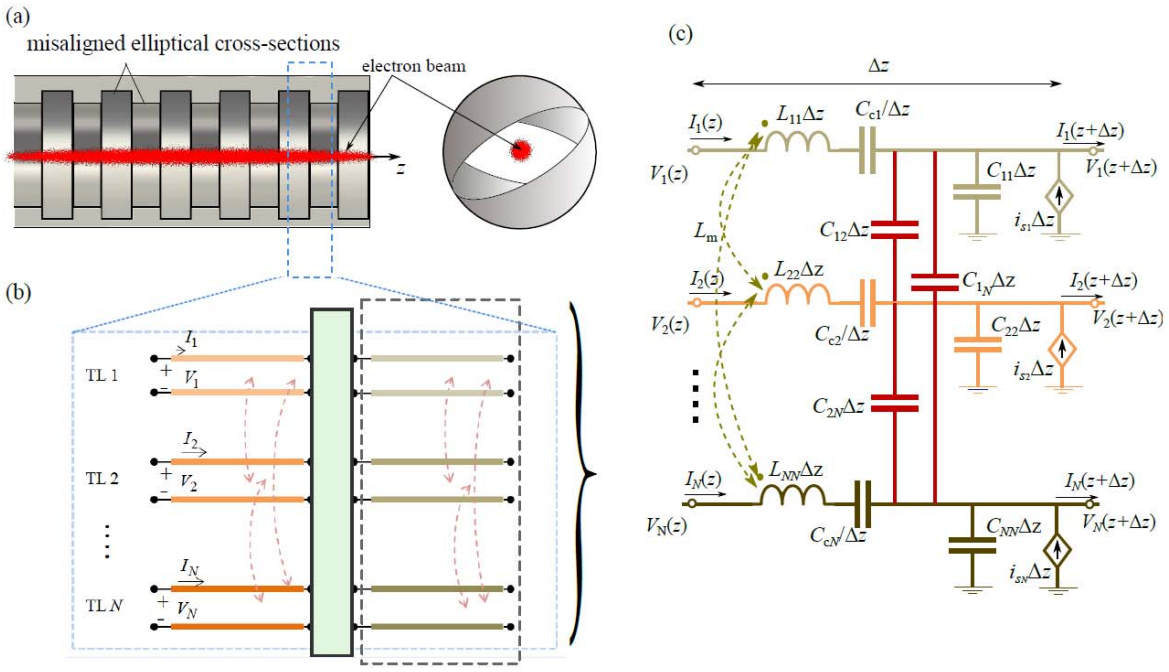

Fig. 2. (a) Example geometry of an SWS comprised periodic misaligned elliptical waveguides that could exhibit EPDs in their "cold" dispersion (see [17]–[19]). (b) CTL equivalent model for the SWS interacting with an electron beam. The example periodic SWS system consists of a unit cell made of three segments of CTLs. A coupling matrix is used to represent the interface between contiguous segments (misaligned elliptical waveguides). (c) Distributed circuit model of one segment of CTL, showing self, coupling, and "cutoff" components (represented by a series capacitance in each TL), as well as the electron beam seen as a dependent current generator that provides energy to the CTL (see [17], [42] for more details).

and currents in a transmission line (TL) that describes the propagation along the z-direction [17], [39]. The transverse electric and magnetic fields are expanded in terms of eigenwaves of the local uniform waveguide as $\mathbf{H}_t(\mathbf{r}) = \sum_n I_n(z)\mathbf{h}_n(x, y)$ and $\mathbf{E}_t(\mathbf{r}) = \sum_n V_n(z)\mathbf{e}_n(x, y)$, where $\mathbf{e}_n(\boldsymbol{\rho})$ and $\mathbf{h}_n(\boldsymbol{\rho})$ are the electric and magnetic modal transverse eigenfunctions, respectively, and V_n and I_n are the amplitudes of those fields that describe the evolution of EM waves along the z-direction (equivalent voltages and currents in the equivalent TLs). We then represent wave propagation in a uniform segment of the waveguide as N-CTLs, or shortly as N-CTLs. Limiting the discussion to N most representative eigenmodes, we use CTL voltage and current vectors defined as $\mathbf{V}(z) = [\, V_1(z)\ V_2(z)\ \cdots\ V_N(z)\,]^T$ and $\mathbf{I}(z) = [\, I_1(z)\ I_2(z)\ \cdots\ I_N(z)\,]^T$, where T denotes the operation of transposition. The subscripts refer to quantities in the nth TL as seen in Fig. 2(b). Therefore, using a phasor representation and $\exp(j\omega t)$ time notation, the evolution of TL voltages and currents are related to each other by the CTL telegrapher equations (see [40, Ch. 3])

$$\begin{aligned}\partial_z \mathbf{V}(z) &= -\left(\underline{\underline{\mathbf{R}}} + j\omega\underline{\underline{\mathbf{L}}} + \frac{1}{j\omega}\underline{\underline{\mathbf{C}}_c}^{-1}\right)\mathbf{I}(z)\\ \partial_z \mathbf{I}(z) &= -\left(\underline{\underline{\mathbf{G}}} + j\omega\underline{\underline{\mathbf{C}}} + \frac{1}{j\omega}\underline{\underline{\mathbf{L}}_c}^{-1}\right)\mathbf{V}(z).\end{aligned} \tag{1}$$

where $\partial_z \equiv \partial/\partial_z$, and $\underline{\underline{\mathbf{L}}}$, $\underline{\underline{\mathbf{C}}}$, $\underline{\underline{\mathbf{R}}}$, $\underline{\underline{\mathbf{G}}}$, $\underline{\underline{\mathbf{C}}_c}$, and $\underline{\underline{\mathbf{L}}_c}$ are $N \times N$ matrices representing the per-unit length inductance, capacitance, loss resistance, loss conductance, cutoff capacitance, and cutoff inductance of the CTL segment [Fig. 2(c)]. The cutoff capacitance (inductance) matrix $\underline{\underline{\mathbf{C}}_c}(\underline{\underline{\mathbf{L}}_c})$ is included in the formulation to represent the cutoff conditions of TM^z (TE^z) eigenmodes in a waveguide (see [41, Ch. 8]) (see [17], [18] for details). In general, CTLs have distributed (i.e., per length) coupling, i.e., the per-unit length CTL matrices $\underline{\underline{\mathbf{L}}}$, $\underline{\underline{\mathbf{C}}}$, $\underline{\underline{\mathbf{R}}}$, $\underline{\underline{\mathbf{G}}}$, $\underline{\underline{\mathbf{C}}_c}$, and $\underline{\underline{\mathbf{L}}_c}$ have off-diagonal elements representing inductive or capacitive coupling between TLs. Coupling between eigenwaves can occur in a distributed fashion but also at the interface between two TL segments as the one shown in Fig. 2(a) and (b), and mathematically it has been described by a rotation matrix as in [17], [18], and [25].

It is convenient to describe the evolution of waves in the SWS system in Fig. 2(a) by a space varying N-dimensional state vector composed only of the field quantities that vary along the z-direction, which are the TL voltage and current vectors

$$\boldsymbol{\Psi}(z) = \begin{bmatrix}\mathbf{V}(z)\\ \mathbf{I}(z)\end{bmatrix}. \tag{2}$$

Then, the set of equations in (1) describing the evolution of the CTL voltages and currents in space are conveniently rewritten as a first-order differential equation in the form

$$\partial_z \boldsymbol{\Psi}(z) = -j\underline{\underline{\mathbf{M}}}(z)\boldsymbol{\Psi}(z) \tag{3}$$

where $\underline{\underline{\mathbf{M}}}(z)$ is the $2N \times 2N$ system matrix that describes all the z-dependent "cold" CTLs. Losses are included in this description [42]. Within each segment of the unit cell in Fig. 2, we assume that $\underline{\underline{\mathbf{M}}}(z)$ is z-invariant, corresponding to a uniform waveguide cross section. Therefore, within each segment $\underline{\underline{\mathbf{M}}}$ is independent of z, and the solution of (3) is in the form $\boldsymbol{\Psi}(z) = \exp[-j(z - z_0)\underline{\underline{\mathbf{M}}}]\boldsymbol{\Psi}(z_0)$ with $\boldsymbol{\Psi}(z_0)$ being a boundary condition at coordinate z_0 in the same segment or at its boundary. The $2N \times 2N$ transfer matrix of each CTL

segment is then constructed as $\underline{\mathbf{T}}(z, z_0) = \exp(-j(z - z_0)\underline{\mathbf{M}})$. A unit cell of the periodic SWS in Fig. 2 may be formed by multiple segments with matrix $\underline{\mathbf{M}}_s$, with $s = \{1, 2, .., S\}$. As such, the boundaries z_s and z_{s+1} of each segment are related through a transformation of the state vector using the transfer matrix as

$$\mathbf{\Psi}(z_{s+1}) = \underline{\mathbf{T}}(z_{s+1}, z_s)\mathbf{\Psi}(z_s) = \underline{\mathbf{T}}_s\mathbf{\Psi}(z_s). \tag{4}$$

We also assume that reactive coupling produced by evanescent fields that may be excited at interface discontinuities in Fig. 2 are approximately accounted for in the distributed TL parameters, since the TL segments are electrically short. Therefore, the transfer matrix of the unit cell $\underline{\mathbf{T}}_{\mathrm{U}}$ is obtained by cascading the transfer matrices of individual segments using the group properties of the transfer matrix [12].

In summary, the transfer matrix approach for an N-dimensional state vector leads to a $2N \times 2N$ transfer $\underline{\mathbf{T}}_{\mathrm{U}}$ matrix for the unit cell of the SWS. Across the unit cell of a periodic SWS, the system vector evolves as

$$\mathbf{\Psi}(z + d) = \underline{\mathbf{T}}_{\mathrm{U}}\ \mathbf{\Psi}(z) \tag{5}$$

where d is the period (see Figs. 1 and 2). Periodic Floquet–Bloch solutions for such system satisfy the equation $\mathbf{\Psi}(z + d) = \zeta\mathbf{\Psi}(z)$, where $\zeta = e^{-jkd}$ and k is the Floquet–Bloch wavenumber in the cold periodic structure. The Floquet–Bloch wavenumber k is obtained from the following eigenvalue problem for the eigenvalues and the regular eigenvectors at a certain z as

$$\underline{\mathbf{T}}_{\mathrm{U}}\ \mathbf{\Psi}_n(z) = \zeta\mathbf{\Psi}_n(z) \tag{6}$$

such that the $2N$ eigenvalues $\zeta = \zeta_n = e^{-jk_nd}$ and $\zeta = \zeta_n' = e^{jk_nd}$ of $\underline{\mathbf{T}}_{\mathrm{U}}$, with $n = 1, 2, \ldots, N$, are obtained as solutions of the characteristic equation $\det(\underline{\mathbf{T}}_{\mathrm{U}} - \zeta\underline{\mathbf{1}}) = 0$ where $\underline{\mathbf{1}}$ is the $2N \times 2N$ identity matrix, while $\{\mathbf{\Psi}_1(z), \mathbf{\Psi}_2(z), \ldots, \mathbf{\Psi}_N(z)\}$ is the set of regular eigenvectors that constitute a basis for $\underline{\mathbf{T}}_{\mathrm{U}}$; hence, they are linearly independent. We introduce the matrix $\underline{\underline{\mathbf{k}}}$ as an $N \times N$ diagonal matrix, whose diagonal elements are the Floquet–Bloch wavenumbers with positive real values, i.e., $\underline{\underline{\mathbf{k}}} = \mathrm{diag}(k_1, k_2, \ldots, k_N)$. In fact, note that k_n and $-k_n$, with $n = 1, 2, \ldots, N$, are the Floquet–Bloch wavenumbers for the periodic structure because we consider reciprocal SWSs. This transfer matrix approach is used to obtain both the Floquet–Bloch eigenwave dispersion for an infinitely long cold CTL and to calculate the transfer function for CTL with finite length interacting with the electron beam that will be derived in Section IV. The main focus in the following is to explore EPDs manifesting in such SWSs, and later we investigate their interaction with the electron beam for applications in oscillators and amplifiers.

B. Exceptional Points of Degeneracy

The EPD is the point in the parameter space of the SWS at which $\underline{\mathbf{T}}_{\mathrm{U}}$ in (5) is not diagonalizable yet similar to a matrix that contains one or more Jordan blocks. The EPD is associated with repeated eigenvalues, and multiple eigenvectors coalescing to form a degenerate eigenvector. At the EPD, the eigenvectors and the generalized eigenvectors [12], [43] are found, not from the typical eigenvalue problem in (6) but rather by solving

$$(\underline{\mathbf{T}}_{\mathrm{U}} - \zeta\underline{\mathbf{1}})^q\mathbf{\Psi}_q(z) = \mathbf{0}, \quad q = 1, 2, \ldots, m \tag{7}$$

where $\mathbf{\Psi}_q$ is the generalized eigenvector and m is the order of degeneracy, i.e., the number of coalescing eigenvectors at the degeneracy point denoted by m. We will investigate the cases when $m = 4$ (DBE) or $m = 3$ (SIP). The transfer matrix $\underline{\mathbf{T}}_{\mathrm{U}}$ in (4) and (5) is not diagonalizable, and $\underline{\mathbf{T}}_{\mathrm{U}}$ is rather similar to a matrix contain Jordan blocks as

$$\underline{\mathbf{T}}_{\mathrm{U}} = \underline{\mathbf{W}}\,\underline{\mathbf{\Lambda}}\,\underline{\mathbf{W}}^{-1}, \quad \underline{\mathbf{\Lambda}} = \begin{pmatrix} \underline{\underline{\mathbf{\Lambda}}} & & \underline{\underline{\mathbf{0}}} & \\ & \underline{\underline{\mathbf{J}}}_1 & \underline{\underline{\mathbf{0}}} & \underline{\underline{\mathbf{0}}} \\ \underline{\underline{\mathbf{0}}} & \underline{\underline{\mathbf{0}}} & \ddots & \underline{\underline{\mathbf{0}}} \\ & \underline{\underline{\mathbf{0}}} & \underline{\underline{\mathbf{0}}} & \underline{\underline{\mathbf{J}}}_M \end{pmatrix}. \tag{8}$$

Here, $\underline{\mathbf{W}}$ is a nonsingular similarity transformation whose $\underline{\underline{\mathbf{J}}}_i$, $i = 1, 2, \ldots, M$ are a set of Jordan blocks corresponding to various EPDs that can coexist at the same point in the parameter space of the SWS. These Jordan blocks may have different sizes corresponding to different orders of EPDs. For example, a fourth-order EPD (i.e., the DBE) corresponds to a 4×4 Jordan matrix

$$\underline{\underline{\mathbf{J}}} = \begin{pmatrix} \zeta_e & 1 & 0 & 0 \\ 0 & \zeta_e & 1 & 0 \\ 0 & 0 & \zeta_e & 1 \\ 0 & 0 & 0 & \zeta_e \end{pmatrix} \tag{9}$$

where $\zeta_e = e^{-jk_ed}$ in (9) is the EPD eigenvalue of multiplicity m and $\underline{\mathbf{W}}$ columns are the possible regular and generalized eigenvectors. A remarkable feature of a Jordan block is that its matrix exponential yields an off-diagonal term that is proportional to ze^{-jk_ez}, $z^2e^{-jk_ez}$, $z^3e^{-jk_ez}$, ..., which provides an unusual wave propagation characteristic that pertains only to the EPD. In the following, we investigate the characteristics of a fourth-order EPD occurring in cold periodic structure, namely, the DBE, and show some of its giant resonance characteristics and also its experimental verification.

III. Fourth-Order EPDs (DBEs) Characteristics in Cold SWSs

Here, we focus on the characteristics of a fourth-order EPD (DBE) in a periodic SWS in a specific geometry. Yet we stress that the DBE can be achieved in many other periodically loaded structures currently used in TWT vacuum technology and can be readily scaled to desired frequencies as seen in Section V, for millimeter-wave and terahertz frequencies.

In Fig. 3(a), we show an example of a metal circular waveguide, periodically loaded with metal elliptical rings, which supports a DBE. The two successive rings have an angular misalignment φ between their major axes in the xy plane, as shown in Fig. 3(a). Therefore, the unit cell of length d consists of two elliptical rings, and all the physical parameters' values are provided in [44]. A DBE condition in the periodic structure's dispersion can be designed by tuning the misalignment angle φ, while all the other physical parameters are kept fixed (see more detailed discussion in [19]). The elliptical rings provide means for the anisotropic behavior (in the xy plane)

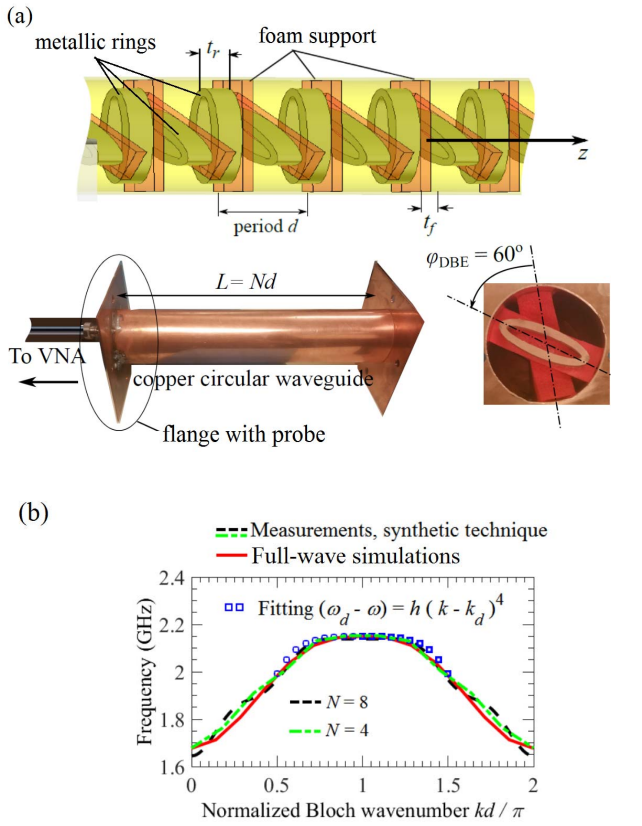

Fig. 3. (a) Geometry of a periodically loaded circular waveguide under study that exhibits a DBE. The metal circular waveguide is loaded with elliptical metal rings with a designed misalignment angle of $\varphi_{DBE} = 60°$. The rings are supported by a low-index dielectric that is not affecting mode propagation. A coaxial probe is inserted on the vertical metallic wall at a distance r_p from the waveguide axis. (b) Synthesized dispersion relation of the waveguide in Figs. 1 and 3 based on reflection measurements of S_{11}, showing the propagation wavenumber versus frequency. This is in good agreement with the one obtained via full-wave simulations and with the characterizing DBE fitting dispersion law $(\omega_d - \omega) = h_{DBE}(k - k_d)^4$ with $h_{DBE} = 435.57$ rad $\cdot$ m^4/s. Data are taken from [44].

and, therefore, are able to support two polarizations in the SWS, which, when coupled while propagating along the z-direction, are able to develop a DBE, i.e., a degeneracy between four eigenwaves at the band edge. The typical DBE dispersion relation (when losses are negligible) is given by

$$D_{DBE}(\omega, k) \approx (\omega_d - \omega) - h_{DBE}(k - k_d)^4 = 0 \qquad (10)$$

where ω_d here corresponds to a frequency of 2.16 GHz and h_{DBE} is a fitting constant that depends on the geometry and plays a fundamental role in engineering the eigenmode dispersion since it identifies the flatness of the dispersion at ω_d [45].

For the waveguide in Fig. 3(a), a DBE condition, when (10) is satisfied numerically, is found when $\varphi = \varphi_{DBE} \cong 60°$, assuming negligible losses. To provide an experimental verification of the DBE, the waveguide in Fig. 3 is fabricated from copper along with the rings. (Therefore, losses and fabrication tolerances of this hand-mounted lab prototype are present.) We use a synthetic method [46] based on the measurement of the resonant frequencies of the finite-length cavity formed

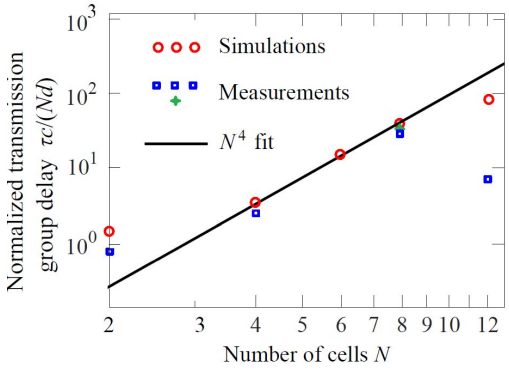

Fig. 4. Scaling of the normalized transmission group delay defined as $\tau = -\partial(\angle S_{21})/\partial\omega$ where $\angle S_{21}$ is the phase of S_{21} parameter, measured for different lengths (number of unit cells) of the waveguide. The result from full-wave simulation is also shown demonstrating good agreement with the measurements and the theoretical scaling trend N^4 for large N. However, measurements of group delay for $N = 12$ are affected by losses that tend to limit the characteristic DBE features for long waveguides. The star symbol represents a measurement after dismantling and reassembling the waveguide for $N = 8$, confirming the practicality of realizing the DBE in waveguides.

in Fig. 3(a). Such synthetic method utilizes a fitting algorithm to estimate the corresponding Bloch phase shift $k(\omega)d$ varying as a function of frequency. The dispersion is estimated by taking into account the number of observed resonances in the frequency band of interest (see detailed procedure in [44]). We report in Fig. 3(b) the comparison between full-wave simulation of the periodic waveguide (assuming negligible losses) using the finite-element method eigenmode solver (in CST Microwave Studio) and the corresponding prototype measurement using the synthetic technique of the $N = 8$ cell cavity described earlier. A very good agreement between simulations and measurements is demonstrated in Fig. 3.

We show in Fig. 4 the measured transmission group delay of the waveguide at the DBE resonance. The transmission group delay is defined as $\tau = -\partial(\angle S_{21})/\partial\omega$ where $\angle S_{21}$ is the phase of S_{21} scattering parameter and it is obtained by performing a numerical derivative of measured phase data. In Fig. 4, the group delay associated with transmission is shown for different lengths of the waveguide, from measurements and full-wave simulations, normalized by the free space delay Nd/c. Measurements and simulations are in good agreement, and the normalized group delay relates to the unprecedented scaling trend N^4 for large N as predicted from theoretical calculations [16]. We also show the measured group delay after dismantling and reassembling the waveguide with $N = 8$ unit cells, shown by the star symbol in Fig. 4, which indicates that our results are easily reproducible in the same setup. Note that the group delay by itself scales as Q following the trend

$$\tau \propto N^5, \quad Q \propto N^5 \qquad (11)$$

and the normalized group delay $\tau c/(Nd)$ scales as N^4. In summary, the DBE is a condition that can be obtained is a rather simple multimodal waveguide without the necessity of very accurate fabrication methods and is tolerant to losses in practical structures.

IV. Generalized Pierce Theory for Multimodal SWS With Degeneracies Interacting With an Electron Beam

In order to investigate the interaction of an electron beam with the EM waves in structures such as those in Figs. 1 and 2, we adopt an CTL approach that extends the single-mode hydrodynamical interaction theory developed by Pierce and contemporaries [47]–[50] to the multimode interaction (generalized Pierce model) as was done in [17], [42], and [51]. We assume that the electron beam has a very small cross section, and that it is infinite along the z-direction, neglecting any transverse motion of electrons and fringing effects due to the structure's finite length. This allows treating the electron beam as a smoothed-out flow of charges [42], [48]. All other assumptions are also stated in [17]. The interaction of SWS modes with an electron beam is taken into account by investigating the induced charge waves as in [42] and [48]. Such charge wave describes the bunching and debunching of electrons, which cause energy exchange between the beam and the modes in the SWS. The electron beam has an average (dc) current $-I_0$ along the z-direction (I_0 is the positive real number), and a dc equivalent beam kinetic voltage V_0 that is related to the average electron velocity u_0 by $V_0 = u_0^2/(2\eta)$. Here, $\eta = e/m$ is the electron charge-to-mass ratio, and $-e$ and m refer to the charge and mass of the electron, respectively. The EM fields in the waveguide induce a perturbation (modulation or disturbance) on the electron beam [48] described by a modulation of the charge wave current I_b and modulation of beam velocity u_b with an equivalent kinetic voltage modulation $V_b = u_0 u_b/\eta$ [17], [42], with the same frequency as the EM fields in the SWS. Therefore, the total beam current is $-I_0 + I_b$ with $|I_b| \ll I_0$ and the total equivalent beam voltage is $V_0 + V_b$ with $|V_b| \ll V_0$, based on small-signal considerations. The model can also conveniently adapt to the realistic properties of the waveguide such as the DBE mode distribution (by considering the transverse field eigenmodes in each waveguide segment [17]). We define the plasma frequency ω_p, as $\omega_p^2 = n_v e\eta/\varepsilon_0 = 2V_0 u_0/(\varepsilon_0 A)$ with n_v being the volumetric electron density, and A is the beam cross-sectional area. When the beam area is finite (corresponding to nonvanishing plasma frequency), the self-generated forces within the electron beam causes debunching of electrons or the space-charge effect.

The evolution along the z-direction of the time-harmonic EM wave [described in terms of N-TL voltages and currents as in Fig. 2(b) and (c)] as well as the charge wave current and voltage modulations, I_b and V_b, respectively, are described using our CTL approach [17], [18], [42] based on the following CTL-beam evolution equations

$$\begin{aligned}
\partial_z \mathbf{V}(z) &= -\left[j\omega \underline{\underline{\mathbf{L}}}(z) + \underline{\underline{\mathbf{R}}}(z) - j\frac{1}{\omega}\underline{\underline{\mathbf{C}}_c}^{-1}(z) \right] \mathbf{I}(z) \\
\partial_z \mathbf{I}(z) &= -j\omega \underline{\underline{\mathbf{C}}}(z)\, \mathbf{V}(z) - \partial_z[\mathbf{s}(z) I_b(z)] \\
(j\omega + u_0\partial_z) V_b(z) &= +u_0 \partial_z[\mathbf{a}^T(z)\mathbf{V}(z)] - j\frac{2V_0\omega_p^2}{I_0\omega} I_b(z) \\
(j\omega + u_0\partial_z) I_b(z) &= j\omega \frac{I_0}{2V_0} V_b(z).
\end{aligned} \tag{12}$$

The last two equations in (12) describe the charge wave dynamics coupled to the CTL through the coupling coefficients $\mathbf{a}$ and $\mathbf{s}$ between the charge wave and the TL fields (refer to [17] and [42] for details). For simplicity, in the following, we choose $\mathbf{a}^T = \mathbf{s}^T = [1 \;\; 1 \;\; \cdots \;\; 1]$ which means that all TLs interact with the charge wave. Analogously to what was done in (2), we conveniently define a space varying state vector of dimension $2(N+1)$ composed only of the field quantities that vary along the z-direction, which are the TL voltage and current vectors (2), as well as the charge wave current and voltage modulations, I_b and V_b, respectively,

$$\mathbf{\Psi}_b(z) = \left[\mathbf{V}^T(z) \quad \mathbf{I}^T(z) \quad V_b(z) \quad I_b(z) \right]^T. \tag{13}$$

We rewrite the equations in (12), in analogy to the procedure for the cold structure, as a first-order partial differential equation

$$\partial_z \mathbf{\Psi}_b(z) = -j\underline{\mathbf{M}}_b(z)\mathbf{\Psi}_b(z) \tag{14}$$

where $\underline{\mathbf{M}}_b(z)$ is the $2(N+1) \times 2(N+1)$ system matrix that describes all the z-dependent CTL, electron beam, and space-charge parameters, including coupling effects and losses (see [42]). We then generalize the procedure done in Section II to obtain the transfer matrix of the unit cell of the hot structure as well as the eigenmodes supported by such interactive system. The main capability of the CTL approach summarized above (thoroughly detailed in [17], [18], [25], and [42]) is to unveil a new interaction scheme that leads to a super-synchronization between the electron beam and a number of degenerate eigenwaves in an SWS. Next, we summarize the properties of two hot structures based on fourth- and third-order EPD, namely, the DBE and the SIP, respectively.

A. Four-Eigenmode Supersynchronization at the DBE and Low-Starting Current

As we have shown above, the SWSs depicted as those in Figs. 1–3 do support a DBE with four-degenerate Floquet–Bloch eigenwaves. We would like to point out that each of the four Bloch eigenwave can be decomposed in infinitely many Floquet–Bloch harmonics as shown in [17]. In the "cold" SWS, four Floquet–Bloch harmonics have wavenumbers $k_n^p = \pi/d + F_p$, with $F_p = 2\pi p/d$, where $p = 0, \pm 1, \pm 2, \ldots$ is the index of the Floquet–Bloch harmonic. Only a slow harmonic is phase-synchronized with the electron beam having average velocity u_0, which we refer to it with $p = 0$ index. Hence, there are four slow Floquet–Bloch harmonics with identical wavenumbers $k_d = \pi/d$ at the band-edge angular frequency ω_d, and the supersynchronism condition can be represented by the following equality:

$$u_0 \approx \frac{\omega_d}{k_d} = \frac{\omega_d d}{\pi}. \tag{15}$$

The condition (15) is the necessary preliminary criterion for the oscillation scheme proposed in this premise based on the fourth-order EPD synchronization. By solving (15) for the desired u_0, which is depicted graphically in Fig. 1(b) by intersecting the "cold" structure dispersion and the beamline $\omega(k) = ku_0$ at the Brillouin zone edge, one can obtain the

main necessary recipe for obtaining the fourth-order EPD supersynchronization mechanism.

Compared to the one of the pure DBEs in the cold SWS, the dispersion diagram of the hot structure (not shown here) is somewhat perturbed for small electron-beam current I_0 (see [17] for more details), but it is significantly distorted for large beam currents. This implies that strictly speaking one may lose the degeneracy for large electron-beam currents. However, as is observed in the complex dispersion diagrams pertaining to "hot" structures in [59, Figs. 6 and 11] and in [17, Figs. 7, 9, 11, and 15], even though the mathematical "exact" degeneracy is not observed, there are three or four EM modes, respectively, that are interacting with the electron beam. It must be noted that these four eigenmodes carry identical EM polarizations at the exact degeneracy of the cold structure (indeed, they are exactly a single degenerate mode); therefore, it is expected that even in the perturbed degeneracy in the hot structure, some polarization similarity among these modes is preserved. The degree of perturbation depends on the amount of electron-beam current and if the current becomes very strong, there could be almost no memory of the original degeneracy. Therefore, depending on the strength of the electron-beam current, advantageous characteristics still occur since the multimode structure of four eigenwaves interacting with the electron beam is still there though the precise advantage should be verified numerically.

We provide below an example of the consequences of the fourth-order EPD synchronization in hot SWSs by estimating the oscillation threshold. The threshold condition current also known as the starting-oscillation beam current $I_{\rm st}$ is defined as the minimum value of the electron-beam current that can initiate oscillations. In an infinitely long structure with the e-beam as a source of linear gain, the EM waves exhibit either unbounded growing oscillations in time at every fixed point in space or growing oscillations only in space, i.e., progressing along z; those instabilities are commonly referred to as absolute and convective instabilities, respectively (see [52], [53]). Criteria for these two distinct instabilities in an infinitely periodic interactive system can be drawn from investigating the dispersion diagram thereof following the Briggs–Bers condition (see [54, Ch. 2], [55, Ch. 2]). Finite-length structures with internal amplification (i.e., convective instability) could start to oscillate. Growing oscillations in that case could occur when amplified waves provide constructive interference with the positive feedback after reflections at the two ends of the SWS with gain. Condition for such occurrence of oscillations in a finite-length structure is examined by tracing the location of the poles of the transfer function in the complex angular frequency ω-plane as a function of the electron-beam current I_0, as typically done for BWOs (see [56], and also details in [25]).

We then report the starting current of a DBEO in Fig. 5 for a lossless structure circular waveguide, periodically loaded with perfect electrical conductor elliptical rings, which supports a DBE with the precise misalignment angle to generate a DBE. It is important to note that these DBEO design parameters here are different from the one shown in Fig. 3, and all the parameters of this DBEO example are reported in [25].

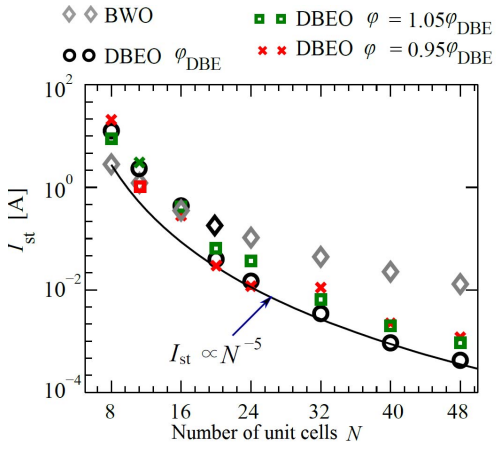

Fig. 5. Starting beam current (oscillation threshold current) for the DBEO, made of a lossless SWS with DBE, varying as a function of TL length Nd, under supersynchronous condition (15). We also show starting current results for two cases with angles misaligned with respect to the DBE condition whose $\varphi_{\rm DBE} = 68.8°$ [25] (the structure design parameters used here are different from the one in Fig. 3). The starting current follows the trend $I_{\rm st} \approx \alpha/N^5$ with $\alpha = 9 \times 10^4$ [A]. For comparison purposes, the starting current for a BWO of the same length is also plotted. The BWO has a much higher starting current. Data are taken from [25].

We also show the starting with two misalignment parameters φ deviations from the corresponding DBE design, varying as a function of the number of unit cells N. We have found that the optimal design with $\varphi = \varphi_{\rm DBE}$ demonstrates the lowest starting current. The other two cases with slight deviation from $\varphi_{\rm DBE}$ also show low starting current but the starting current for the optimal design is the lowest. We also demonstrate the anomalous threshold current trend for large N, for the DBE case, by plotting the fitting curve

$$I_{\rm st} = \frac{\alpha}{N^5}. \tag{16}$$

The fitting curve agrees with the threshold current values obtained by the analysis based on transfer matrix discussed previously when N is large (i.e., $N > 16$) which indicates that the starting current for the DBE case scales as $\propto 1/N^5$. This demonstrates the recently discovered scaling law of the threshold current [25]. This also poses possible great advantage of utilizing DBE in high-power oscillators when increasing the length especially for high frequencies as shown in Section V. The reasons for such unconventional scaling are that Q-factor for DBE scales as in (11) (see [12], [15], [16] for details). For the sake of comparison, we then also calculate the starting current in a standard BWO of the same length and with interaction impedance Z equal to the average impedance of the CTL in Fig. 2, which scales as $I_{\rm st} \propto N^{-3}$ [57], [58]. We observe that for structures with the number of unit cells such that $N > 16$, the starting current of the DBE is lower than that of a BWO. Especially, for $N = 48$ unit cells, the starting current is 2 orders of magnitude lower than that of a standard BWO.

B. Three-Mode Supersynchronization at the SIP

We investigate another interesting synchronization occurring in SWSs near the third-order EPD, namely, the SIP [59]. In this case, simultaneous synchronization of the charge wave modulating the electron beam with three Floquet–Bloch eigenwaves

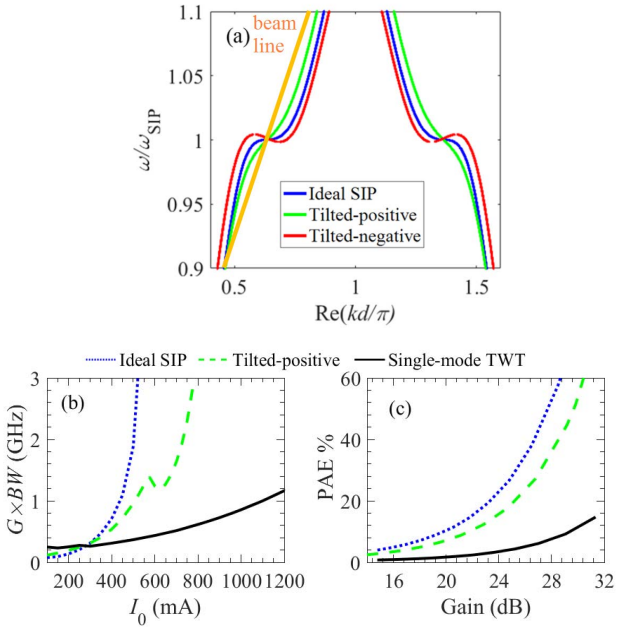

Fig. 6. (a) Engineering the slope of the dispersion diagram leads to local positive and negative slopes (group velocities) compared to the ideal SIP case that has vanishing group velocity (blue lines). The synchronous condition is represented with the intersection with the beamline, used to conceive a new amplification regime. (b) Hot simulations showing the gain–bandwidth product ($G \times$ BW) for an ideal SIP and tilted-positive regimes of TWT operation, compared with a single-mode TWT, having the same characteristic impedance, length, and loading plotted versus the beam current. (c) PAE in percentage for the three regimes as a function of the TWT power gain (in decibel). Data are taken from [59].

with positive phase velocity along the $+z$-direction occurs in a periodic SWS. As discussed in [43], the SIP in the cold periodic, lossless, and structure has a dispersion relation that, in the neighborhood of ω_{SIP}, is approximated by a third-order polynomial in k as

$$D_{\text{SIP}} \approx (\omega - \omega_{\text{SIP}}) - h_{\text{SIP}}(k - k_{\text{SIP}})^3 = 0 \tag{17}$$

where ω_{SIP} is the angular frequency at which three eigenwaves coalesce, h_{SIP} is the third-order EPD flatness parameter depending on the chosen SWS parameters, and k_{SIP} is the Floquet–Bloch wavenumber at the SIP. As such, near the SIP angular frequency ω_{SIP}, there are three eigenwaves with distinct Floquet–Bloch wavenumbers k provided by (17). Two of which have complex conjugate wavenumbers and thus representing evanescent waves, growing, and decaying along the $+z$-direction, while the third one has a purely real Floquet–Bloch wavenumber and thus represents a propagating wave in the lossless SWS [the one shown in Fig. 6(a)] [59]. The plot also shows the so-called "beamline" given by the charge wave dispersion relation $(u_0 k - \omega)^2 = 0$, where u_0 is the average speed of the electrons in the electron beam [47], [48]. The three-eigenmode synchronous interaction occurs when the beamline is chosen to intersect the SIP as seen graphically in Fig. 6(a). A three-eigenmode synchronization with the electron beam [59] is then established when the phase velocity of the eigenmodes in the SWS equals the velocity u_0 of electrons, i.e., in the proposed regime, the TWT design formula [59] is

$$u_0 \approx \omega_{\text{SIP}}/k_{\text{SIP}}. \tag{18}$$

We utilize here the three CTLs model in Fig. 2(c) to mimic the dispersion of an SWS with SIP, with three CTLs (see details in [59]). The series capacitance model cutoff frequencies in metallic waveguides (see [41, Ch. 8]). The generalized Pierce theory developed in [17], [18], and [42] allows the electron beam to interact with multiple waves in an SWS. Analogous to the fourth-order EPD case in Fig. 1(b); here, the three-eigenwave synchronous interaction occurs when the beamline is chosen to intersect the SIP as seen graphically in Fig. 6(a). Such regime has the following major advances: 1) a significant gain enhancement of the proposed TWT with SIP in comparison with a periodic single-mode Pierce model (orders of magnitude higher gain for the same length and/or the same dc power supplied); 2) substantial gain–bandwidth product improvement for SIP schemes; and 3) significantly higher power efficiency (especially for high power gain values) compared to a single-mode Pierce TWT modeled with one TL [59].

One important feature of the proposed scheme is that the slope of the dispersion relation can be engineered for enhancing the bandwidth. After some algebraic manipulations, the dispersion relation in (17) can be engineered to achieve a tilted slope, as a deviation from the ideal SIP [59]. For the tilted SIP, the dispersion can be approximated as a perturbation of $D_{\text{SIP}}(\omega, k)$ as

$$\begin{aligned} D_{\text{SIP,titled}} &\cong D_{\text{SIP}} - v_t k \\ &= (\omega - \omega_{\text{SIP}}) - a(k - k_{\text{SIP}})^3 - v_t k = 0 \end{aligned} \tag{19}$$

where v_t is the minimum group velocity of tilted SIP cases, which occurs at the original SIP wavenumber $k = k_{\text{SIP}}$. By tuning the SWS parameters, we can engineer the dispersion diagram to have small positive group velocities ($\partial\omega/\partial k > 0$) or small negative group velocities ($\partial\omega/\partial k < 0$) around the SIP frequency instead of the ideal case with zero group velocity (see [59]). The dispersion diagrams of the three cases near the SIP frequency are shown in Fig. 6(a) where we obtain a positive slope (green curve) and negative slope (red curve) group velocities around the SIP by inducing small variations in the SWS design based on the three CTLs (see [59]). Locally negative slopes associated with the tilted regimes would be beneficial for oscillators (absolute instability regimes), while slightly positive slope is useful for amplifiers (convective instability regimes) as shown in the following.

As an important figure of merit for amplifiers, we plot in Fig. 6(b) the gain–bandwidth product ($G \times$ BW) results for the ideal SIP and the tilted-positive amplification regimes as compared to that of the periodic single TL pierce model versus electron-beam current. In Fig. 6(b), the $G \times$ BW is defined as the product of the maximum power gain and the 3-dB-gain bandwidth. The results of Fig. 6(b) show that both the SIP amplification regimes outperform the conventional regime based on the single TL Pierce model, for electron-beam currents larger than $I_0 = 300$ mA where the gain is high enough to be desirable for amplifier applications.

Finally, we report another important parameter for amplifiers, the power-added efficiency (PAE), which is defined

(in percentage) as

$$\text{PAE} = (P_{\text{out(RF)}} - P_{\text{in(RF)}})/P_{\text{dc}} \times 100 \tag{20}$$

where P_{dc} is the dc electron-beam power whereas $P_{\text{in(RF)}}$ and $P_{\text{out(RF)}}$ are the input and total output RF powers, respectively. We observe that when comparing the three regimes with equal gain, the larger the required beam current I_0 for a given gain value, the smaller is the PAE. Hence, the SWS beam regime that requires the smaller beam current, at equal gain, has the largest PAE. In Fig. 6(c), we show the PAE for the three SWS regimes mentioned above versus the power gain. (Power gain is varied by changing the electron-beam current I_0.) We report that amplifiers based on the SIP regimes of operation feature significantly higher PAE compared to the amplifier based on the single TL regime of operation, in particular at large power gains.

V. EPDs for High-Power Millimeter and Terahertz Generation

Millimeter-wave and terahertz generation have recently seen a growing interest and progress thanks to the advancement in microfabrication techniques [10], [11], [60] as well as in solid-state devices [61], [62]. Amplifiers and oscillators in this frequency range are vital for many applications that require portable, compact, and lightweight devices for imaging, sensing, and detection [63], [64]. They are also crucial for the advancement of various fronts of science [11], [63], [65]–[67]. However, electron-beam-based vacuum devices typically produce high EM power that scales as the inverse of the frequency-squared [11], [60], [68]. This put a limitation on the attainable power when frequency increases, i.e., at millimeter-wave and terahertz frequencies, using vacuum sources. Moreover, realizing high interaction impedance and avoiding spurious resonances in TWTs and BWOs is a challenge at those frequencies due to losses, misalignment in fabrications, as well as the overmoded nature of some of those devices. Special dispersion engineering must be performed to attain higher levels of power and better efficiencies [1], [11], [60], [68]. The EPD framework may present an avenue for potential improvement in output power and efficiency compared to conventional devices at millimeter-wave and terahertz frequencies.

Here, we present a preliminary investigation of SWSs at millimeter wave and terahertz that exhibit an EPD. In particular, we demonstrate a DBEO at 638 GHz based on CST Particle Studio, 3-D particle-in-cell (PIC) simulator.

A. Cylindrical Waveguide With Periodically Corrugated Surface

The structure in Fig. 7 is a cylindrical waveguide whose inner walls are periodically patterned in both the longitudinal and azimuthal directions, and it is referred to as periodic surface lattice and has been proposed for BWO operation in [69] and [70]. The cylindrical waveguide walls are periodically patterned in both the z-direction and ϕ-direction such that the inner radius of the waveguide is $r = r_0 + \Delta r \cos(\beta z)\cos(l\phi)$ where r_0 is the mean radius of the unperturbated cylindrical waveguide, Δr is the amplitude of the perturbation, l is an integer representing the number of azimatul variations, and $\beta = 2\pi/d$, with d being the lattice longitudinal period. Such corrugated waveguide allows coupling between the surface eigenwaves supported by the corrugations and the cylindrical waveguide eigenmodes as shown in [69]. Here, we show the eigenmode dispersion relation between the propagation Bloch wavenumber and the angular frequency (i.e., $k-\omega$ relation) of the periodic structure whose parameters are given in Fig. 7. The dispersion diagram in Fig. 7(d) has been calculated using the finite-element method, implemented in the eigenmode solver of CST Microwave Studio. The corrugated waveguide structure is overmoded as seen from Fig. 7(d) meaning that there are many propagating eigenwaves existing at different bands of frequencies, especially in the range between 40 and 45 GHz. However, some eigenmodes can be seen to exhibit flat dispersion near the band edge at $kd = \pi$, as shown from the dotted fitting lines in the dispersion plot in Fig. 7(d). Such observation can be beneficial to engineer the output mode distribution and may lead to high-efficient operation when synchronized with an electron beam at the DBE.

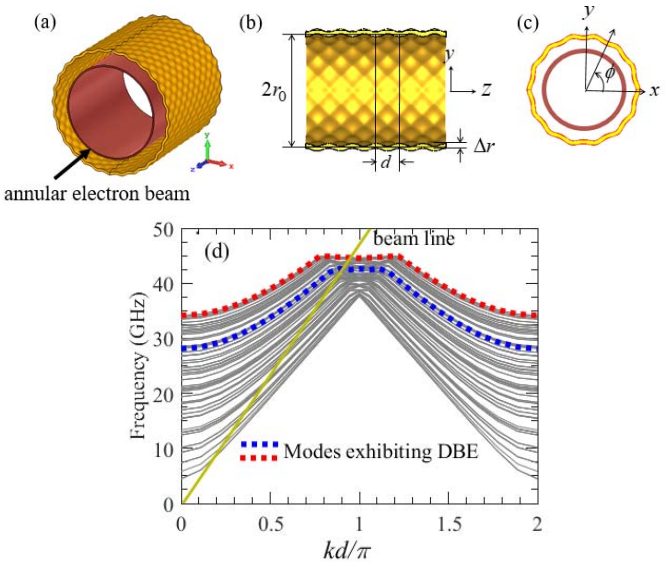

Fig. 7. Schematics of periodic surface lattice on a cylindrical waveguide's inner wall, i.e., where inner radius is perturbated. (a) 3-D perspective view, (b) longitudinal cut, and (c) transverse cross sections of such waveguide with corrugations, adapted from [69]. This structure can support a DBE. This specific geometry is compatible with annular electron beams. (d) Dispersion relation of modes in the waveguide showing an overmoded behavior and possible DBEs (showing in dotted lines) exhibiting flat dispersion in the millimeter-wave frequency range. Here, the parameters are $r_0 = 19.75$ mm, $\Delta r = 0.25$ mm, and $d = 4$ mm.

B. Periodic Double-Corrugated Waveguide and the Degenerate Band-Edge Oscillator

Another potential SWS geometry at millimeter-wave or terahertz frequencies considered is the double-corrugated rectangular waveguide [71], [72] shown in Fig. 8. Note that the SWS has two identical parallel sets of corrugations assembled in a rectangular waveguide such that they create a channel suitable for interaction with a cylindrical electron beam.

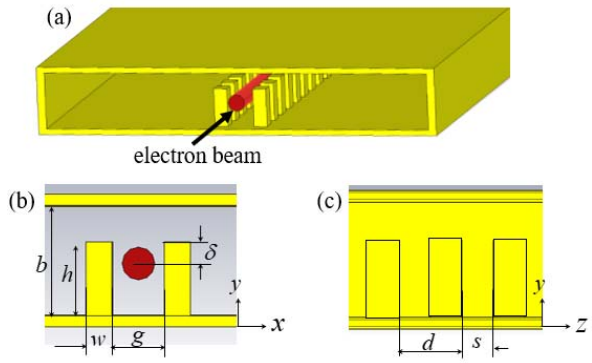

Fig. 8. Schematics of double corrugations inside a rectangular waveguide. (a) 3-D perspective view. (b) Transverse cross section, in the xy plane. (c) yz cross sections (i.e., a side view). This structure is adapted from [71] and will be used as a basis for a modified structure to realize a DBEO at terahertz frequencies (see Fig. 9).

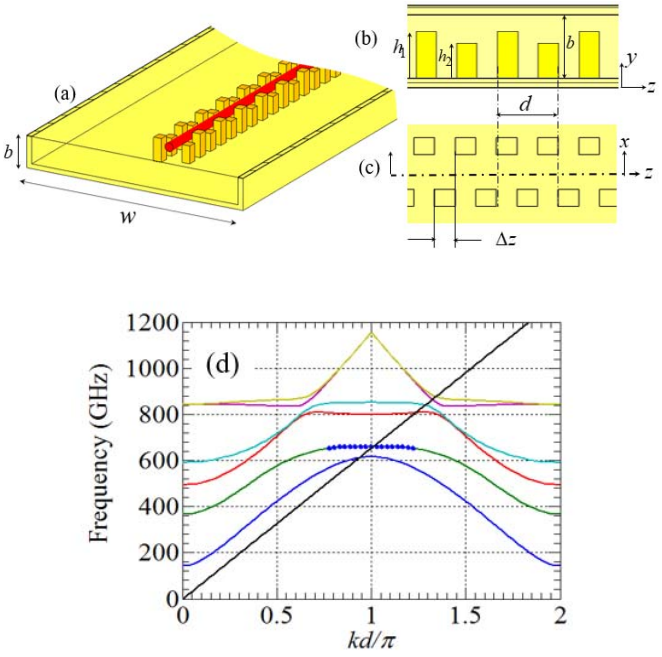

Fig. 9. Proposed double-corrugated waveguide with DBE. (a) 3-D perspective view. (b) Lateral view, i.e., the yz cross section. Here, the ridges along the z-direction have different heights h_1 and h_2. (c) Top view, i.e., the xz cross section showing the offset Δz in the z-direction between the two parallel corrugations. (d) Dispersion relation of the first few eigenmodes for the modified double-corrugated waveguide showing normalized propagation wavenumber versus frequency. The second mode (green curve) exhibits a DBE at 661 GHz, proved by the fitting dispersion law $(\omega_d - \omega) \cong h_{\mathrm{DBE}}(k - k_d)^4$ (blue dotted line). The beamline "black line" intersects with the DBE eigenwaves curve at around DBE frequency. This is used to conceive a DBEO.

In fact, the double-corrugated waveguide may have several potential advantages as stated in [71] and [72], in contrast to typical millimeter-wave and terahertz structures [73], [74]. The structure is here modified to exhibit the DBE as follows. We introduce misalignment between the two parallel corrugations. This misalignment is necessary to have the sufficient mode mixing between the eigenwaves supported by the corrugations so that a DBE occurs. Note that in the geometry proposed in [71] and shown in Fig. 8, the eigenwaves appear as symmetric and antisymmetric pairs [71]. The corrugation misalignment enables a mode-mixing scheme leading to new set of eigenwaves that exhibit a DBE. There are two degrees of misalignment introduced here: 1) the two parallel corrugations are misaligned by an offset Δz in the z-direction as shown in Fig. 9(c) and 2) the corrugation height alternates periodically, between two different values h_1 and h_2 as shown in Fig. 9(b).

We optimize the design parameters (Δz, h_1, and h_2) such that a DBE is manifested at 661 GHz. The resulting values are reported in Table I. Fig. 9(d) shows the dispersion relation of the first few order modes in the SWS calculated using the finite-element method eigenmode solver implemented by CST Microwave Studio. The dispersion relation shows that the second mode is asymptotically equivalent to the ideal dispersion (10) where here $h_{\mathrm{DBE}} = 5.55$ rad $\cdot$ m^4/s. The lower frequency mode exhibits a regular band edge, which is the standard band-edge condition in periodic structures, whereas the higher order mode exhibits a DBE. In the following, we consider the four-degenerate eigenwave interaction regime by requiring that the velocity of the beam electrons must match the phase velocity of a Floquet harmonic of the four waveguide eigenwaves at DBE frequency (i.e., condition (15)). In other words, the designs start by selecting a beam electron velocity u_0 such that the "beamline" intersects the "cold" structure dispersion diagram around the DBE point in Fig. 9.

In Fig. 10, we show the longitudinal electric field component E_z of the DBE mode at different transverse cross sections through the unit cell. The DBE mode field profile exhibits both symmetric and asymmetric features because it is a mix between symmetric and asymmetric modes due to the introduced misalignment. In summary, the E_z field has alternating positive and negative values as necessary to interact with the electron beam.

TABLE I

DIMENSIONS AND PARAMETERS OF THE DOUBLE-CORRUGATED WAVEGUIDE WITH DBE

Symbol	Quantity	Value (μm)
w_r	Ridge width	30
g	Ridge lateral separation	60
d	Period	70
s	Ridges longitudinal separation	35
w	Waveguide width	800
b	Waveguide height	115
Δz	Offset in z-direction	35
h_1, h_2	Heights of ridges	85, 64

The DBEO based on the double-corrugated SWS to oscillate at a frequency in the neighbor of the DBE frequency is designed with a solid electron beam with voltage of $V_0 = 77.13$ kV and current of $I_0 = 20$ mA. The beam radius is $r_{\mathrm{beam}} = 25$ μm. We use a longitudinal magnetic field of 2 T, and the number of unit cells is 90, corresponding to an SWS length of 12.6 mm. The metal of the SWS is considered to be copper with conductivity $\sigma = 5.9 \times 10^7$ $\Omega^{-1} \cdot$ m^{-1} as in [71]. The waveguide is terminated by a beam collector, and the terahertz signal power is extracted from the cathode side through output coupling section identical to the setup in [73], for simplicity. In Fig. 11, we show the results of DBEO using CST Particle Studio, PIC simulator, and observe that

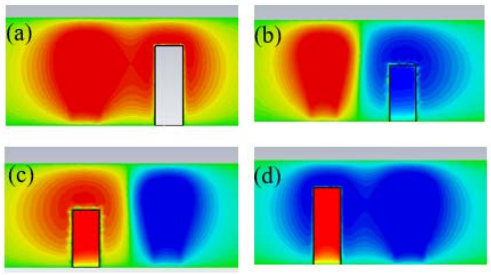

Fig. 10. Electric field $\underline{E}_z$ profile of the DBE eigenwave at 661 GHz, at different transverse cross sections (i.e., in the xy plane, at different z-coordinates) in the unit cell starting from $z = 0$: (a) $z = 0.1d$, (b) $z = 0.4d$, (c) $z = 0.6d$, and (d) $z = 0.9d$, where d is the period. Blue and red indicate the negative and positive values of the $\underline{E}_z$ field, at a given time.

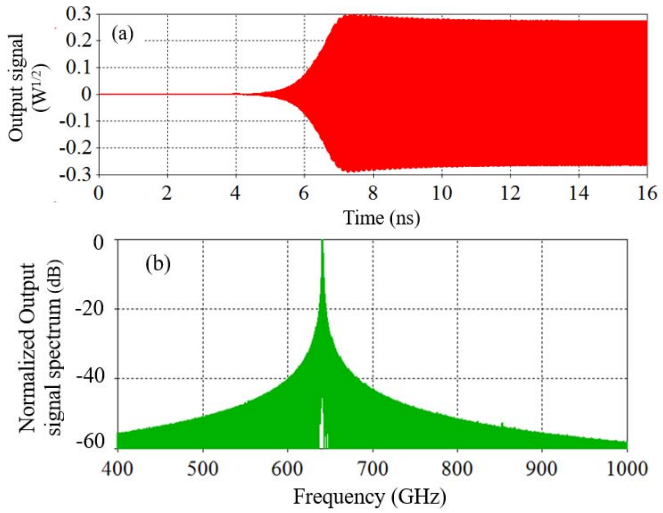

Fig. 11. (a) Oscillating output signal versus time of the DBEO made of a modified double-corrugated waveguide shown in Fig. 9. Steady oscillation regime is reached at approximately 7 ns. (b) Normalized spectrum of the output signal shows that the oscillations occur at 638 GHz, which indicates that the oscillations are approximately at the DBE frequency. The spectrum is calculated in a time window from 14 to 15 ns.

the DBEO has a well-defined single-frequency output signal at 638 GHz. This frequency is in close proximity of the DBE frequency. The small difference may be due to the fact that a finite-length SWS exhibits a DBE resonant frequency at a frequency slightly lower than the DBE one, as observed in [25].

These preliminary results show a great promise in adopting such geometry to generate high power at terahertz frequencies, and more investigations are required to improve the interaction impedance between the beam and DBE eigenwaves, and also to better understand the role of metal losses at this frequency. Other geometries could also be investigated employing concepts in metamaterials [75] and multichannel waveguides that can also designed to exhibit high orders of EPDs by increasing the number of channels.

VI. Conclusion

We have summarized a framework for novel high-power electron-beam devices based on EPD, such as the DBE and the SIP, with fourth and third degeneracy orders, respectively. An EPD, having concurrent multiple eigenwaves, causes enhanced interaction with the electron beam and offers new advantages in terms of power generation at microwave frequencies, through millimeter-wave and terahertz frequencies. We have shown a unique scheme for amplification in SWSs with EPDs. Using an EPD in electron-beam devices results in an efficient generation of high-power radiation as we have shown from an example, unprecedented scaling in the starting current of oscillators, as well as large gain–bandwidth product and higher added power efficiency in amplifiers. We have also demonstrated for the first time millimeter-wave- and terahertz-based high-power SWSs with EPD that potentially could be used to enhance the efficiency of sources at those frequencies. By choosing an example at terahertz waves, we have provided the first evidence based on PIC simulations that the DBE leads to an oscillator with single frequency of oscillation approximately at the DBE frequency. This result is in agreement with a recent contribution by some of the authors where the DBE was used to conceive a new lasing regime based on the four-light eigenmode interaction with quantum states of matter [76]. Future studies in the realm of electron-beam devices to prove advantages from the exploitation of the proposed multi-eigenmode interaction scheme should focus on the design of realistic structures paying attention to the interaction impedance. Indeed, it is not obvious to conceive an SWS that involves four coalescing modes, with such coalescence preserving the desired longitudinal electric field for a proper electron-beam EM mode interaction. The preliminary example shown in this paper, though not representing an optimized structure for high efficiency, shows the first example where the control of eigenmodes for both a fourth-order degeneracy and a proper longitudinal field distribution is possible.

Acknowledgment

The authors would like to thank Prof. E. Schamiloglu, University of New Mexico, Albuquerque, NM, USA, for useful discussions. They would like to thank Dr. M. Shapiro and Prof. R. Temkin, MIT, Cambridge, MA, USA. They would also like to thank the Computer Simulation Technology, GmbH, for providing CST Microwave Studio and Particle Studio that were instrumental in this work.

References

[1] J. Benford, J. A. Swegle, and E. Schamiloglu, *High Power Microwaves*. Boca Raton, FL, USA: CRC Press, 2015.
[2] S. E. Tsimring, *Electron Beams and Microwave Vacuum Electronics*, vol. 191. Hoboken, NJ, USA: Wiley, 2006.
[3] M. Zuboraj, N. Apaydin, K. Sertel, and J. L. Volakis, "Half-ring helical structure for traveling wave tube amplifiers," *IEEE Trans. Plasma Sci.*, vol. 42, no. 11, pp. 3465–3470, Nov. 2014.
[4] R. Lipton and A. Polizzi, "Tuning gain and bandwidth of traveling wave tubes using metamaterial beam-wave interaction structures," *J. Appl. Phys.*, vol. 116, no. 14, p. 144504, 2014.
[5] J. S. Hummelt, S. M. Lewis, M. A. Shapiro, and R. J. Temkin, "Design of a metamaterial-based backward-wave oscillator," *IEEE Trans. Plasma Sci.*, vol. 42, no. 4, pp. 930–936, Apr. 2014.
[6] S. C. Yurt, M. I. Fuks, S. Prasad, and E. Schamiloglu, "Design of a metamaterial slow wave structure for an O-type high power microwave generator," *Phys. Plasmas*, vol. 23, no. 12, p. 123115, 2016.
[7] Y. S. Wang *et al.*, "S-band high-efficiency metamaterial microwave sources," *IEEE Trans. Electron Devices*, vol. 63, no. 9, pp. 3747–3752, May 2016.

[8] X. Tang *et al.*, "Dual band metamaterial Cherenkov oscillator with a waveguide coupler," *IEEE Trans. Electron Devices*, vol. 64, no. 5, pp. 2376–2382, May 2017.

[9] U. Chipengo, N. K. Nahar, and J. L. Volakis, "Backward-wave oscillator operating in low magnetic fields using a hybrid-TE_{11} mode," *IEEE Trans. Electron Devices*, vol. 64, no. 9, pp. 3863–3869, Sep. 2017.

[10] R. L. Ives, "Microfabrication of high-frequency vacuum electron devices," *IEEE Trans. Plasma Sci.*, vol. 32, no. 3, pp. 1277–1291, Jun. 2004.

[11] S. S. Dhillon *et al.*, "The 2017 terahertz science and technology roadmap," *J. Phys. D, Appl. Phys.*, vol. 50, no. 4, p. 043001, 2017.

[12] A. Figotin and I. Vitebskiy, "Gigantic transmission band-edge resonance in periodic stacks of anisotropic layers," *Phys. Rev. E, Stat. Phys. Plasmas Fluids Relat.*, vol. 72, no. 3, p. 036619, Sep. 2005.

[13] C. Löcker, K. Sertel, and J. L. Volakis, "Emulation of propagation in layered anisotropic media with equivalent coupled microstrip lines," *IEEE Microw. Wireless Compon. Lett.*, vol. 16, no. 12, pp. 642–644, Dec. 2006.

[14] A. Figotin and I. Vitebskiy, "Slow wave phenomena in photonic crystals," *Laser Photon. Rev.*, vol. 5, no. 2, pp. 201–213, Mar. 2011.

[15] N. Gutman, C. M. de Sterke, A. A. Sukhorukov, and L. C. Botten, "Slow and frozen light in optical waveguides with multiple gratings: Degenerate band edges and stationary inflection points," *Phys. Rev. A, Gen. Phys.*, vol. 85, no. 3, p. 033804, Mar. 2012.

[16] M. A. K. Othman, F. Yazdi, A. Figotin, and F. Capolino, "Giant gain enhancement in photonic crystals with a degenerate band edge," *Phys. Rev. B, Condens. Matter*, vol. 93, no. 2, p. 024301, 2016.

[17] M. Othman, V. A. Tamma, and F. Capolino, "Theory and new amplification regime in periodic multi modal slow wave structures with degeneracy interacting with an electron beam," *IEEE Trans. Plasma Sci.*, vol. 44, no. 4, pp. 594–611, Apr. 2016.

[18] M. A. K. Othman, M. Veysi, A. Figotin, and F. Capolino, "Giant amplification in degenerate band edge slow-wave structures interacting with an electron beam," *Phys. Plasmas*, vol. 23, no. 3, p. 033112, 2016.

[19] M. A. K. Othman and F. Capolino, "Demonstration of a degenerate band edge in periodically-loaded circular waveguides," *IEEE Microw. Wireless Compon. Lett.*, vol. 25, no. 11, pp. 700–702, Nov. 2015.

[20] M. G. Wood, J. R. Burr, and R. M. Reano, "Degenerate band edge resonances in periodic silicon ridge waveguides," *Opt. Lett.*, vol. 40, no. 11, pp. 2493–2496, 2015.

[21] J. L. Volakis and K. Sertel, "Narrowband and wideband metamaterial antennas based on degenerate band edge and magnetic photonic crystals," *Proc. IEEE*, vol. 99, no. 10, pp. 1732–1745, Oct. 2011.

[22] M. B. Stephanson, K. Sertel, and J. L. Volakis, "Frozen modes in coupled microstrip lines printed on ferromagnetic substrates," *IEEE Microw. Wireless Compon. Lett.*, vol. 18, no. 5, pp. 305–307, May 2008.

[23] M. R. Lamont, B. T. Kuhlmey, and C. M. de Sterke, "Multi-order dispersion engineering for optimal four-wave mixing," *Opt. Express*, vol. 16, no. 10, pp. 7551–7563, 2008.

[24] S. A. Schulz, L. O'Faolain, D. M. Beggs, T. P. White, A. Melloni, and T. F. Krauss, "Dispersion engineered slow light in photonic crystals: A comparison," *J. Opt.*, vol. 12, no. 10, p. 104004, 2010.

[25] M. A. Othman, M. Veysi, A. Figotin, and F. Capolino, "Low starting electron beam current in degenerate band edge oscillators," *IEEE Trans. Plasma Sci.*, vol. 44, no. 6, pp. 918–929, Jun. 2016.

[26] A. Figotin and I. Vitebskiy, "Frozen light in photonic crystals with degenerate band edge," *Phys. Rev. E, Stat. Phys. Plasmas Fluids Relat.*, vol. 74, no. 6, p. 066613, Dec. 2006.

[27] R. El-Ganainy, K. G. Makris, D. N. Christodoulides, and Z. H. Musslimani, "Theory of coupled optical PT-symmetric structures," *Opt. Lett.*, vol. 32, no. 17, pp. 2632–2634, 2007.

[28] A. Guo *et al.*, "Observation of PT-symmetry breaking in complex optical potentials," *Phys. Rev. Lett.*, vol. 103, no. 9, p. 093902, 2009.

[29] C. E. Rüter, K. G. Makris, R. El-Ganainy, D. N. Christodoulides, M. Segev, and D. Kip, "Observation of parity-time symmetry in optics," *Nature Phys.*, vol. 6, no. 3, pp. 192–195, 2010.

[30] H. Hodaei, M.-A. Miri, M. Heinrich, D. N. Christodoulides, and M. Khajavikhan, "Parity-time-symmetric microring lasers," *Science*, vol. 346, no. 6212, pp. 975–978, 2014.

[31] M. A. K. Othman and F. Capolino, "Theory of exceptional points of degeneracy in uniform coupled waveguides and balance of gain and loss," *IEEE Trans. Antennas Propag.*, vol. 65, no. 10, pp. 5289–5302, Oct. 2017.

[32] M. A. K. Othman, V. Galdi, and F. Capolino, "Exceptional points of degeneracy and PT symmetry in photonic coupled chains of scatterers," *Phys. Rev. B, Condens. Matter*, vol. 95, no. 10, p. 104305, Mar. 2017.

[33] T. Kato, *Perturbation Theory for Linear Operators*, vol. 132. Berlin, Germany: Springer, 1995.

[34] W. D. Heiss, "Exceptional points of non-Hermitian operators," *J. Phys. Math. Gen.*, vol. 37, no. 6, p. 2455, 2004.

[35] W. D. Heiss, "The physics of exceptional points," *J. Phys. Math. Theor.*, vol. 45, no. 44, p. 444016, 2012.

[36] D. M. Pozar, *Microwave Engineering*. Hoboken, NJ, USA: Wiley, 2009.

[37] A. Figotin and I. Vitebskiy, "Oblique frozen modes in periodic layered media," *Phys. Rev. E, Stat. Phys. Plasmas Fluids Relat.*, vol. 68, no. 3, p. 036609, Sep. 2003.

[38] A. M. Zuboraj, B. K. Sertel, and C. J. L. Volakis, "Propagation of degenerate band-edge modes using dual nonidentical coupled transmission lines," *Phys. Rev. A, Gen. Phys.*, vol. 7, no. 6, p. 064030, 2017.

[39] N. Marcuvitz and J. Schwinger, "On the representation of the electric and magnetic fields produced by currents and discontinuities in wave guides. I," *J. Appl. Phys.*, vol. 22, no. 6, pp. 806–819, Jun. 1951.

[40] C. R. Paul, *Analysis of Multiconductor Transmission Lines*. Hoboken, NJ, USA: Wiley, 2008.

[41] R. F. Harrington, *Time-Harmonic Electromagnetic Fields*. New York, NY, USA: McGraw-Hill, 1961.

[42] V. A. Tamma and F. Capolino, "Extension of the Pierce model to multiple transmission lines interacting with an electron beam," *IEEE Trans. Plasma Sci.*, vol. 42, no. 4, pp. 899–910, Apr. 2014.

[43] A. Figotin and I. Vitebskiy, "Electromagnetic unidirectionality in magnetic photonic crystals," *Phys. Rev. B, Condens. Matter*, vol. 67, no. 16, p. 165210, 2003.

[44] M. A. K. Othman, X. Pan, Y. Atmatzakis, C. G. Christodoulou, and F. Capolino, "Experimental demonstration of degenerate band edge in metallic periodically-loaded circular waveguid," *IEEE Microw. Theory Techn.*, vol. 65, no. 11, pp. 4037–4045, Nov. 2017.

[45] M. Y. Nada, M. A. K. Othman, O. Boyraz, and F. Capolino, "Giant resonance and anomalous quality factor scaling in degenerate band edge coupled resonator optical waveguides," *J. Lightw. Technol.*, vol. 36, no. 14, pp. 3030–3039, Jul. 15, 2018.

[46] H. Guo *et al.*, "A novel highly accurate synthetic technique for determination of the dispersive characteristics in periodic slow wave circuits," *IEEE Trans. Microw. Theory Techn.*, vol. 40, no. 11, pp. 2086–2094, Nov. 1992.

[47] J. R. Pierce, "Theory of the beam-type traveling-wave tube," *Proc. IRE*, vol. 35, no. 2, pp. 111–123, Feb. 1947.

[48] J. R. Pierce, *Travelling-Wave Tubes*. New York, NY, USA: Van Nostrand, 1950.

[49] R. Kompfner, "The traveling-wave tube as amplifier at microwaves," *Proc. IRE*, vol. 35, no. 2, pp. 124–127, Feb. 1947.

[50] L. J. Chu and J. D. Jackson, "Field theory of traveling-wave tubes," *Proc. IRE*, vol. 36, no. 7, pp. 853–863, Jul. 1945.

[51] A. Figotin and G. Reyes, "Multi-transmission-line-beam interactive system," *J. Math. Phys.*, vol. 54, no. 11, p. 111901, 2013.

[52] P. A. Sturrock, "Kinematics of growing waves," *Phys. Rev.*, vol. 112, no. 5, p. 1488, 1958.

[53] P. Huerre and P. A. Monkewitz, "Local and global instabilities in spatially developing flows," *Annu. Rev. Fluid Mech.*, vol. 22, no. 1, pp. 473–537, 1990.

[54] R. J. Briggs, *Electron-Stream Interaction With Plasmas*. Cambridge, MA, USA: MIT Press, 1964.

[55] A. Bers, *Handbook of Plasma Physics*. New York, NY, USA: North-Holland, 1983.

[56] H. R. Johnson, "Backward-wave oscillators," *Proc. IRE*, vol. 43, no. 6, pp. 684–697, Jun. 1955.

[57] L. R. Walker, "Starting currents in the backward-wave oscillator," *J. Appl. Phys.*, vol. 24, no. 7, pp. 854–859, 1953.

[58] R. Kompfner and N. T. Williams, "Backward-wave tubes," *Proc. IRE*, vol. 41, no. 11, pp. 1602–1611, Nov. 1953.

[59] F. Yazdi, M. A. K. Othman, M. Veysi, A. Figotin, and F. Capolino, "A new amplification regime for traveling wave tubes with third order modal degeneracy," *IEEE Trans. Plasma Sci.*, vol. 46, no. 1, pp. 43–56, Jan. 2018.

[60] J. H. Booske, "Plasma physics and related challenges of millimeter-wave-to-terahertz and high power microwave generation," *Phys. Plasmas*, vol. 15, no. 5, pp. 055502-1–055502-16, May 2008.

[61] L. A. Samoska, "An overview of solid-state integrated circuit amplifiers in the submillimeter-wave and THz regime," *IEEE Trans. THz Sci. Technol.*, vol. 1, no. 1, pp. 9–24, Aug. 2011.

[62] H.-J. Song and T. Nagatsuma, "Present and future of terahertz communications," *IEEE Trans. THz Sci. Technol.*, vol. 1, no. 1, pp. 256–263, Sep. 2011.

[63] J. F. Federici *et al.*, "THz imaging and sensing for security applications—Explosives, weapons and drugs," *Semicond. Sci. Technol.*, vol. 20, no. 7, p. S266, 2005.
[64] R. Appleby and H. B. Wallace, "Standoff detection of weapons and contraband in the 100 GHz to 1 THz region," *IEEE Trans. Antennas Propag.*, vol. 55, no. 11, pp. 2944–2956, Nov. 2007.
[65] B. B. Hu and M. C. Nuss, "Imaging with terahertz waves," *Opt. Lett.*, vol. 20, no. 16, pp. 1716–1718, Apr. 1995.
[66] J. M. Chamberlain and R. Miles, *New Directions in Terahertz Technology*, vol. 334. Berlin, Germany: Springer, 2012.
[67] K. B. Cooper, R. J. Dengler, N. Llombart, B. Thomas, G. Chattopadhyay, and P. H. Siegel, "THz imaging radar for standoff personnel screening," *IEEE Trans. THz Sci. Technol.*, vol. 1, no. 1, pp. 169–182, Jun. 2011.
[68] R. J. Barker, N. C. Luhmann, J. H. Booske, and G. S. Nusinovich, *Modern Microwave and Millimeter-Wave Power Electronics*, vol. 1, R. J. Bark, N. C. Luhmann, J. H. Booske, and G. Nusinovich, Eds. Hoboken, NJ, USA: Wiley, 2005, p. 872.
[69] I. V. Konoplev, A. J. MacLachlan, C. W. Robertson, A. W. Cross, and A. D. R. Phelps, "Cylindrical periodic surface lattice as a metadielectric: Concept of a surface-field Cherenkov source of coherent radiation," *Phys. Rev. A, Gen. Phys.*, vol. 84, pp. 013826-1–013826-12, Jul. 2011.
[70] I. V. Konoplev, A. J. MacLachlan, C. W. Robertson, A. W. Cross, and A. D. R. Phelps, "Cylindrical, periodic surface lattice-theory, dispersion analysis, and experiment," *Appl. Phys. Lett.*, vol. 101, no. 12, p. 121111, Sep. 2012.
[71] M. Mineo and C. Paoloni, "Double-corrugated rectangular waveguide slow-wave structure for terahertz vacuum devices," *IEEE Trans. Electron Devices*, vol. 57, no. 11, pp. 3169–3175, Nov. 2010.
[72] C. Paoloni *et al.*, "THz backward-wave oscillators for plasma diagnostic in nuclear fusion," *IEEE Trans. Plasma Sci.*, vol. 44, no. 4, pp. 369–376, Apr. 2016.
[73] S. Bhattacharjee *et al.*, "Folded waveguide traveling-wave tube sources for terahertz radiation," *IEEE Trans. Plasma Sci.*, vol. 32, no. 3, pp. 1002–1014, Jun. 2004.
[74] J. Cai, J. Feng, and X. Wu, "Folded waveguide slow wave structure with modified circular bends," *IEEE Trans. Electron Devices*, vol. 61, no. 10, pp. 3534–3538, Oct. 2014.
[75] A. Polemi, S. Maci, and P.-S. Kildal, "Dispersion characteristics of a metamaterial-based parallel-plate ridge gap waveguide realized by bed of nails," *IEEE Trans. Antennas Propag.*, vol. 59, no. 3, pp. 904–913, Mar. 2011.
[76] M. Veysi, M. A. K. Othman, A. Figotin, and F. Capolino, "Degenerate band edge laser," *Phys. Rev. B, Condens. Matter*, vol. 97, no. 19, p. 195107, May 2018.

Ahmed F. Abdelshafy was born in Giza, Egypt, in 1991. He received the B.Sc. and M.Sc. degrees in electrical engineering from Cairo University, Giza, in 2012 and 2016, respectively. He is currently pursuing the Ph.D. degree in electrical and computer engineering with the University of California, Irvine, CA, USA.

His current research interests include high-power electromagnetic (EM) sources, microwave and terahertz generation, dispersion engineering, RF bandgap circuits and oscillators, computational EMs, and numerical methods including eigenmode projection techniques and finite-difference time domain.

Mohamed A. K. Othman (S'10–M'18) received the Ph.D. degree from the University of California, Irvine, CA, USA, in 2017.

In 2013, he joined the Institut d'électronique de microélectronique et de nanotechnologie (IEMN), Villeneuve-d'Ascq, France, as a Visiting Student. He is currently a Research Associate with the SLAC National Accelerator Laboratory, Menlo Park, CA, USA. His current research interests include high gradient accelerators, microwave and terahertz generation, ultrafast electron diffraction, dispersion engineering, RF bandgap circuits and oscillators, graphene-based photonics, and numerical methods including eigenmode projection techniques and finite-difference time domain, metamaterials, and plasmonics.

Farshad Yazdi, photograph and biography not available at the time of publication.

Mehdi Veysi, photograph and biography not available at the time of publication.

Alexander Figotin was born in Kharkov, Russia, in 1954. He received the Ph.D. degree in mathematics from Tashkent State University, Tashkent, Russia, in 1980.

He is currently a Professor with the Department of Mathematics, University of California, Irvine, CA, USA. He has authored over 100 papers and several books. His current research interests include the fundamentals of the electromagnetic theory, wave propagation in periodic and random media, theory of linear and nonlinear photonic crystals, and spectral theory of dispersive and dissipative dielectric and other media.

Filippo Capolino (S'94–M'97–SM'04) received the Laurea (*cum laude*) and the Ph.D. degrees in electrical engineering from the University of Florence, Florence, Italy, in 1993 and 1997, respectively.

From 1997 to 1999, he was a Fulbright and then a Post-Doctoral Fellow with the Department of Aerospace and Mechanical Engineering, Boston University, Boston, MA, USA. From 2000 to 2001, part of 2005 and in 2006, he was a Research Assistant Visiting Professor with the Department of Electrical and Computer Engineering, University of Houston, Houston, TX, USA. From 2004 to 2009, he was the EU Coordinator of the EU Doctoral Programs on Metamaterials, European Commission. Since 2003, he has been a short-term Visiting Professor with the Fresnel Institute, Marseille, France. Since 2010, he has been with the Centre de Recherche Paul Pascal, Bordeaux, France. He has been an Assistant Professor with the Department of Information Engineering, University of Siena, Siena, Italy. He is currently a Professor with the Department of Electrical Engineering and Computer Science, University of California, Irvine, CA, USA. His current research interests include metamaterials and their applications, traveling-wave tubes, oscillators, antennas, sensors in microwave and optical ranges, plasmonics, microscopy, wireless systems, millimeter-wave chip-integrated antennas, and applied electromagnetics in general.

Dr. Capolino received the R. W. P. King Prize Paper Award from the IEEE Antennas and Propagation Society for the Best Paper of the Year 2000, by an author under 36. From 2002 to 2008, he served as an Associate Editor for the IEEE TRANSACTIONS ON ANTENNAS AND PROPAGATION. He is currently the Editor of the *Metamaterials Handbook* (Boca Raton, FL, USA: CRC Press, 2009).